MNRAS 000, 1–12 (2020) Preprint 20 February 2024 Compiled using MNRAS LATEX style file v3.0

X-ray properties of He II λ1640 emitting galaxies in VANDELS

A. Saxena,[1,2]★ L. Pentericci,[1] D. Schaerer,[3] R. Schneider,[1,4] R. Amorin,[5,6] A. Bongiorno,[1] A. Calabrò,[1] M. Castellano,[1] A. Cimatti,[7,8] F. Cullen,[9] A. Fontana,[1] J. P. U. Fynbo,[10] N. Hathi,[11] D. J. McLeod,[9] M. Talia[12] and G. Zamorani[12]

[1]*INAF – Osservatorio Astronomico di Roma, via Frascati 33, 00078, Monteporzio Catone, Italy*
[2]*Department of Physics and Astronomy, University College London, Gower Street, London WC1E 6BT, UK*
[3]*Observatoire de Genève, Université de Genève, 51 Ch. des Maillettes, 1290 Versoix, Switzerland*
[4]*Dipartimento di Fisica, Sapienza Università di Roma, Piazzale Aldo Moro 5, 00185, Roma, Italy*
[5]*Instituto de Investigación Multidisciplinar en Ciencia y Tecnología, Universidad de La Serena, Raúl Bitrán 1305, La Serena, Chile*
[6]*Departamento de Física y Astronomía, Universidad de La Serena, Av. Juan Cisternas 1200 Norte, La Serena, Chile*
[7]*University of Bologna, Department of Physics and Astronomy (DIFA), Via Gobetti 93/2, I-40129, Bologna, Italy*
[8]*INAF - Osservatorio Astrofisico di Arcetri, Largo E. Fermi 5, 50125, Firenze, Italy*
[9]*SUPA (Scottish Universities Physics Alliance), Institute for Astronomy, University of Edinburgh, Royal Observatory, EH9 3HJ Edinburgh, UK*
[10]*Cosmic DAWN Center, Niels Bohr Institute, University of Copenhagen, Juliane Maries Vej 30, 2100 Copenhagen Ø, Denmark*
[11]*Space Telescope Science Institute, 3700 San Martin Drive, Baltimore, MD 21218, USA*
[12]*INAF – OAS Bologna, Via P. Gobetti 93/3, 40129, Bologna, Italy*

Accepted 2020 June 18. Received 2020 June 18; in original form 2020 March 30

ABSTRACT

We explore X-ray emission from a sample of 18 He II λ1640 emitting star-forming galaxies at $z \sim 2.3 - 3.6$ from the VANDELS survey in the Chandra Deep Field South, to set constraints on the role of X-ray sources in powering the He II emission. We find that 4 He II emitters have tentative detections with S/N $\sim$ 2 and have X-ray luminosities, $L_X = 1.5 - 4.9 \times 10^{41}$ erg s^{-1}. The stacked luminosity of all 18 He II emitters is 2.6×10^{41} erg s^{-1}, and that of a subset of 13 narrow He II emitters (FHWM(He II) < 1000 km s^{-1}) is 3.1×10^{41} erg s^{-1}. We also measure stacked L_X for non-He II emitters through bootstrapping of matched samples, and find $L_X = 2.5 \times 10^{41}$ erg s^{-1}, which is not significantly different from L_X measured for He II emitters. The L_X per star-formation rate for He II emitters ($\log(L_X/\mathrm{SFR}) \sim 40.0$) and non-emitters ($\log(L_X/\mathrm{SFR}) \sim 39.9$) are also comparable and in line with the redshift evolution and metallicity dependence predicted by models. Due to the non-significant difference between the X-ray emission from galaxies with and without He II, we conclude that X-ray binaries or weak or obscured AGNs are unlikely to be the dominant producers of He II ionising photons in VANDELS star-forming galaxies at $z \sim 3$. Given the comparable physical properties of both He II emitters and non-emitters reported previously, alternative He II ionising mechanisms such as localised low-metallicity stellar populations, Pop-III stars, etc. may need to be explored.

Key words: galaxies: high-redshift – X-rays: binaries – galaxies: evolution

1 INTRODUCTION

Low-mass star-forming galaxies are largely considered to be the key drivers of reionisation, a process through which the Universe made a phase transition from neutral to completely ionised by $z \sim 6$ (Robertson et al. 2010, 2015; Wise et al. 2014; Bouwens et al. 2015). With decreasing metallicities at higher redshifts (Henry et al. 2013; Steidel et al. 2014; Amorín et al. 2017; Sanders et al. 2018; Cullen et al. 2019), galaxies in the early Universe should be capable of producing a large number of ionising photons ($E > 13.6$ eV) and complete the process of reionisation by $z \sim 6$ (Stanway et al. 2016). The metal-free stars (the so-called Pop III stars) in these very early galaxies should have very high masses and temperatures (e.g. Bromm & Larson 2004; Bromm & Yoshida 2011), resulting in the production of hard UV ionising fields that are capable of exciting high-ionisation emission lines, such as He II λ1640, whose ionisation potential is > 54.4 eV or λ < 228 Å (Tumlinson et al. 2001; Schaerer 2003; Scannapieco et al. 2003).

The number of known galaxies that show the high ionisation He II emission line has been steadily growing across redshifts. In the local Universe ($z \sim 0$), the He II λ4868 line is often seen in the spectra of low-mass star-forming galaxies and almost all of them are

★ E-mail: aayush.saxena@ucl.ac.uk

metal-poor (Garnett et al. 1991; Guseva et al. 2000; Izotov & Thuan 2004; Shirazi & Brinchmann 2012; Kehrig et al. 2015, 2018; Berg et al. 2016; Senchyna et al. 2017). Rest-frame UV observations of some of these $z \sim 0$ metal-poor galaxies have revealed the presence of both He II λ1640 as well as C IV λ1540 emission lines (Berg et al. 2019; Senchyna et al. 2020), reinforcing the idea of high ionisation due to massive, metal-poor stars. The samples of He II emitting galaxies at high redshifts have increased too, primarily using lensing (Patrício et al. 2016; Berg et al. 2018) and large-area spectroscopic surveys (Cassata et al. 2013; Nanayakkara et al. 2019; Saxena et al. 2020), leading to detections of He II emitting galaxies out to $z \sim 4$.

Most of the broad He II emission seen across redshifts can be explained primarily through winds driven by Wolf-Rayet (WR) stars (Schaerer 1996). The WR origin in some broad He II emitters (FWHM $>$ 1000 km s^{-1}) has indeed been confirmed through the detection of WR 'bumps' in the spectra of galaxies around the He II and C IV emission lines (Brinchmann et al. 2008; Kehrig et al. 2011; Shirazi & Brinchmann 2012). The inclusion of binary-star evolution in stellar population synthesis (Eldridge et al. 2017; Stanway & Eldridge 2018) results in stars spending longer periods of time in the WR phase, and fits the observed He II line better compared to single-star models (e.g. Steidel et al. 2016). However, not all broad He II emitters, particularly those with low metallicities, may be directly connected with the presence of WR stars (e.g. Shirazi & Brinchmann 2012; Kehrig et al. 2015).

The picture becomes even more complicated when trying to explain the origin of the narrow He II emission line (FWHM $<$ 1000 km s^{-1}) (e.g. Stanway & Eldridge 2019). Some stellar synthesis models including binary stars can reproduce the UV emission line ratios of He II , O III] and C III] of galaxies that show He II λ1640 line observed at high redshifts. However, these models still under-predict the observed equivalent widths (EW) of the He II line (Nanayakkara et al. 2019; Saxena et al. 2020). Other physical mechanisms, such as strong shocks (Dopita & Sutherland 1996; Thuan & Izotov 2005; Izotov et al. 2012), stellar rotation mixing leading to higher effective temperatures (Szécsi et al. 2015), 'stellar stripping' that results in the rejuvenation of old stars that provide extra He II ionising photons (Götberg et al. 2018, 2019), presence of metal-free Pop III stars (Schaerer 2003; Cassata et al. 2013; Visbal et al. 2017), low-level AGN activity (e.g. Mignoli et al. 2019) and contribution from X-ray binaries (XRBs) (Garnett et al. 1991; Stasińska et al. 2015; Kehrig et al. 2015; Schaerer et al. 2019; Senchyna et al. 2020) have been proposed as possible explanations to account for the missing He II ionising photons seen in star-forming galaxies.

XRBs are binary star systems where the production of X-rays is powered by mass transfer from the 'donor' star to a very compact companion, such as a neutron star or black hole, which is called the 'accretor'. The donor star can have a range of masses – when the mass of the donor star is lower than the accretor, the system is referred to as a low-mass XRB. In cases where the donor star is massive, typically a O- or B-type star, the system is referred to as a high-mass XRB. The dominant sources of X-rays from young, star-forming galaxies at high redshifts are generally high-mass XRB systems (e.g. Lehmer et al. 2016). Observations of X-ray emission from star-forming galaxies (at fixed star-formation rates) have revealed a strong metallicity-dependence of their X-ray luminosities. This means that the contribution from XRBs increases with decreasing metallicities (Basu-Zych et al. 2013b; Douna et al. 2015; Brorby et al. 2016; Lehmer et al. 2016; Fornasini et al. 2019). This metallicity dependence of XRBs has also been explored from a theoretical point of view (Linden et al. 2010; Fragos et al. 2013b,a; Madau & Fragos 2017). Especially in the early Universe, when the overall ages and metallicities of galaxies were lower and star-formation rates (SFRs) were higher, X-ray luminosities are also found to correlate strongly with the galaxy SFRs (Basu-Zych et al. 2013a; Lehmer et al. 2016; Aird et al. 2017). This suggests that high-mass XRBs formed in star-forming regions within galaxies are the driving forces behind the observed X-ray luminosities of these galaxies. Since low metallicities and high-mass star-formation are also required to power nebular He II emission, enhanced contribution from XRBs may offer an explanation to the missing He II ionising photons problem (e.g. Schaerer et al. 2019).

Building upon the new sample of He II emitters at $z \sim 2.2 - 5$ that was presented in Saxena et al. (2020, hereafter S20), in this paper we explore their X-ray properties, and compare them with those of the general star-forming galaxy population at similar redshifts. The layout of this paper is as follows: in Section 2 we briefly outline the original sample of He II emitting galaxies and their physical properties. In Section 3 we introduce the X-ray data used in this study and present our methodology for X-ray photometry. In Section 4 we discuss the results of our X-ray analysis, and compare the X-ray properties of He II emitters with samples of non-He II emitters. In Section 5 we present a discussion of our results, and comment on whether X-ray sources play a dominant role in galaxies with He II emission. Finally, we summarise the findings of this paper in Section 6.

Throughout this paper, we assume a ΛCDM cosmology with $\Omega_m = 0.3$ and $H_0 = 67.7$ km s^{-1} Mpc^{-1} taken from Planck Collaboration et al. (2016), and use the AB magnitude system (Oke & Gunn 1983).

2 SAMPLE OF He II EMITTERS FROM VANDELS

2.1 Selection

The sample of He II emitting galaxies considered in this study was first presented in S20, and we refer the readers to this paper for the full description of sample selection, derived physical properties and analysis of both individual and stacked UV spectra. In this section we briefly summarise the key findings of S20. The galaxies were selected from VANDELS (Pentericci et al. 2018; McLure et al. 2018), which is a recently completed deep VIMOS survey of the CANDELS CDFS and UDS fields (Grogin et al. 2011; Koekemoer et al. 2011) carried out using the *Very Large Telescope (VLT)*. We shortlisted a total of 50 star-forming galaxies over a redshift range $z = 2.2 - 4.8$ that showed He II emission in their spectra. Of these, 33 were classified as *Bright* He II emitters where the signal-to-noise ratio (S/N) of the He II emission line was greater than 2.5, and 17 were classified as *Faint* emitters with S/N(He II) $<$ 2.5. Out of the 50 total shortlisted He II emitters, 26 (19 *Bright* and 7 *Faint*) lie in the Chandra Deep Field South (CDFS) and 24 (14 *Bright* and 10 *Faint*) lie in UKIDSS Ultra Deep Survey (UDS) field.

2.2 Physical properties

Physical parameters such as stellar masses, star-formation rates (SFRs), and rest-frame absolute UV magnitudes (M_{UV}) were obtained by fitting spectral energy distribution (SED) templates to photometric points from broad-band filters at the spectroscopic redshift of each galaxy. The SED fits were performed using $Z = 0.2$ $Z_\odot$ metallicity versions of the standard Bruzual & Charlot (2003) models with redshifts fixed to the VANDELS spectroscopic redshift. The star-formation rates were corrected for dust adopting the

Calzetti et al. (2000) dust attenuation law. The rest-frame magnitudes were calculated using a 200 Å wide top-hat filter centred at 1500 Å. We refer the readers to McLure et al. (2018) for full details of the SED fitting techniques, model assumptions, and derived physical parameters for VANDELS sources.

Overall, S20 found that galaxies that show He II emission have comparable stellar masses, star-formation rates and UV magnitudes, to similarly selected VANDELS galaxies with no He II emission over the same redshift range. S20 reported that the stellar mass range of He II emitters is $\log_{10} M_\star = 8.8 - 10.7\ M_\odot$, the UV-corrected star-formation rate (SFR) range is $\log_{10}(\mathrm{SFR}) = 0.7 - 2.3\ M_\odot\ \mathrm{yr}^{-1}$ and the absolute UV magnitude range is $M_{UV} = -21.9$ to -19.2. Two sample Kolmogorov-Smirnov (KS) tests showed that the physical properties of He II emitters are not significantly different from those that do not show He II emission in their spectra.

Next, UV emission line ratio diagnostics (He II λ1640, O III] λ1666, C III] λ1909) were used to study the underlying physical conditions in star-forming galaxies that show He II emission. Line ratios from both single-star models (Gutkin et al. 2016) and binary-star models (Xiao et al. 2018) were used for this analysis. The comparison with models was performed using emission line ratios determined from individual galaxy spectra where the relevant UV lines were detected at high enough S/N, as well as stacks of spectra. In total, three additional stacked spectra were produced: (a) a stack of all *Faint* He II emitters, (b) stack of galaxies in the *Bright* sample that show narrow He II (FWHM < 1000 km s^{-1}), and (c) stack of galaxies in the *Bright* sample that show broad He II (FWHM > 1000 km s^{-1}).

From comparing the line ratios, S20 found that individual He II emitters (with detections of other UV lines) largely favour sub-solar stellar metallicities and low stellar ages. From line ratios of stacked spectra, S20 inferred that the stacks of faint, and bright and narrow He II emitters favour lower metallicities compared to the line ratios from the stack of bright and broad He II emitters. This is in line with predictions based on He II ionising photons being produced in Wolf-Rayet (WR) stars (see Shirazi & Brinchmann 2012, for example) – higher metallicity stellar populations have more stars in the WR phase, which give rise to broad He II emission lines due to strong stellar winds.

For individual galaxies with bright He II emission, as well as for the stack of faint and narrow He II emitters, S20 found that although binary-star models do a reasonably good job at reproducing the line ratios, they under-predict the He II EWs. This means that these models are unable to produce the number of He II ionising photons required to power the observed emission line strengths, and additional sources of ionising photons may be required. S20 argued that there are several mechanisms that could be producing these missing photons, including sub-dominant AGN, stripped stars and/or X-ray binaries (XRBs), particularly the high-mass XRBs, as previously mentioned.

An effective way to investigate the impact of sub-dominant AGN or enhanced contribution from XRBs is to study the X-ray emission from He II emitting galaxies. In Section 3 we describe the available X-ray data and our X-ray photometry methodology.

2.3 This work - the CDFS sample

In this study, we focus on the He II emitting galaxies in the CDFS field. Since the primary goal of this study is to measure X-ray fluxes from He II emitters, access to ultra-deep X-ray data is essential. Therefore, we have chosen to restrict this analysis to the CDFS field, owing to the availability of *Chandra* data with a total of 7 Ms of exposure time. Although *Chandra* data is also available in the UDS field[1], the effective exposure time of the data available in UDS is ∼ 600 ks. This is quite shallow compared to data in the CDFS field and to detect faint star-forming galaxies at high redshifts, the depths reached by 600 ks of exposure time will not be sufficient. More details on X-ray data are given in the following section.

Table 1. Number of sources and breakdown in terms of He II line properties for sources in CDFS.

Class	Property	Number
CDFS X-ray footprint	All He II	21
	Excluding AGN	18
Bright	S/N(He II) > 2.5	12
Faint	S/N(He II) < 2.5	6
Narrow	FWHM(He II) < 1000 km s^{-1}	13
Broad	FWHM(He II) > 1000 km s^{-1}	5

There are a total of 26 He II emitters from S20 (both *Bright* and *Faint* sources) that lie in the CDFS field. Out of these, 21 lie within the X-ray image footprint with high effective exposure times. We then cross-match the positions of He II emitters with the CDFS 7 Ms source catalogue from Luo et al. (2017), using a radius of 2 arcseconds. Magliocchetti et al. (2020) showed that the CDFS catalogue is complete down to X-ray luminosities of 10^{42} erg s^{-1} at $z \sim 3$, and above these luminosities only AGN are found. Therefore, all sources that have a counterpart in the CDFS source catalogue are likely to be X-ray AGN. We do not find any matches between the He II emitters and sources in the CDFS catalogue.

Of the 21 sources within the X-ray footprint, 3 were classified as potential AGN by S20 owing to the presence of strong C IV emission in their spectra. Interestingly, these 3 possible AGN are also not detected in the CDFS 7Ms catalogue. However, to be consistent with S20 we take a conservative approach and remove these three sources from our sample.

The final sample, therefore, consists of 18 He II emitters from S20. Out of these, 12 are *Bright* He II emitters, and 6 are *Faint* He II emitters. Based on the width of the He II line, 13 have narrow (FWHM < 1000 km s^{-1}) and 5 have broad (FWHM > 1000 km s^{-1}) He II lines. The rest-frame UV spectra of He II emitting galaxies can be found in S20. A breakdown of the number of sources and their classification based on their He II line properties is given in Table 1.

3 X-RAY ANALYSIS

3.1 Data

We use X-ray data from the *Chandra X-ray Observatory* in CDFS, which has a total of 7 Ms of exposure time covering an area of ∼ 485 arcmin^2 collected over a period of more than a decade (Luo et al. 2017)[2], making it the deepest X-ray data set in any extragalactic field. Additional data products in the CDFS include the effective exposure map and the PSF map, which are used for aperture photometry. More details about the data reduction and products

[1] http://www.mpe.mpg.de/XraySurveys/XUDS/

[2] The images and catalogues are publicly available at http://personal.psu.edu/wnb3/cdfs/cdfs-chandra.html

in the CDFS field that have been used in this study can be found in Giallongo et al. (2019).

3.2 X-ray photometry of He II emitters

To estimate X-ray fluxes for the 18 He II emitters within the CDFS footprint, we use the 0.8 – 3 keV band image because of two reasons. First, as Giallongo et al. (2019) showed, using the 0.8 – 3 keV image instead of the standard soft X-ray band of 0.5–2 keV results in higher number of counts recovered due to the higher transmissivity of the 0.8 – 3 keV band. Second, the redshift distribution of the sources in this study is such that the 0.8 – 3 keV band comes closest to rest-frame energy range of 2 – 10 keV, upon which the analysis of this paper as well as several other observational studies that will be used for comparison are based. Therefore, the uncertainties arising from the application of k-corrections are minimised.

We measure the X-ray flux of He II emitters by performing aperture photometry using PHOTUTILS (Bradley et al. 2019) at the RA and Dec of each source, taken from the VANDELS catalogue. Our methodology to measure the source and background counts for individual sources is as follows. We place a circular aperture encompassing the effective Chandra PSF (median diameter of 3.0″) at the positions of each He II emitter to measure the total number of counts from the source. To measure the local background, we place a circular annulus with inner radius of 10″ and outer radius of 20″, centred on the same position as the circular aperture. Within the annulus, we mask pixels that are brighter than 4σ – a relatively conservative value – so as not to overestimate the background. Within the circular aperture and the annulus, we measure the total number of counts from the source and the background, $C_{\rm gal}$ and $C_{\rm bkg}$, the area encompassed, $A_{\rm gal}$ and $A_{\rm bkg}$ (pixel^2), and the effective exposure times, $t_{\rm gal}$ and $t_{\rm bkg}$ (seconds), respectively. We follow Fornasini et al. (2019) and calculate the background subtracted counts as

$$C_{\rm bkgsub} = C_{\rm gal} - C_{\rm bkg} \times \left(\frac{A_{\rm gal} \times t_{\rm gal}}{A_{\rm bkg} \times t_{\rm bkg}} \right) \quad (1)$$

Since the counts from individual galaxies at these redshifts are expected to be low, we use Gehrels (1986) approximation to establish confidence limits for a Poissonian distribution, which is standard practice when calculating errors in cases of low photon counts.

To convert from background subtracted counts in the 0.8 – 3 keV band to X-ray flux in the standard 2 – 10 keV band, which was selected to facilitate comparison with other similar studies, we must assume a spectral model to calculate the effective photon energy ($E_{\rm eff}$) in the band and the appropriate k-correction ($k_{\rm corr}$). In line with similar studies in the literature (e.g. Brorby et al. 2016), we assume a model with an un-obscured power-law spectrum with photon index $\Gamma = 2.0$ and a galactic extinction value of $5{\times}10^{20}$ cm^{-2} (van de Voort et al. 2012), which is the average value observed for star-forming galaxies at high redshifts inferred from cosmological simulations. We then use PIMMS[3] to calculate $E_{\rm eff}$ required to convert counts in the observed frame 0.8 – 3 keV band to fluxes in the observed frame 2–10 keV energy range. We calculate X-ray fluxes in the 2 – 10 keV range ($F_{\text{2-10 keV}}$) by dividing background subtracted counts by the effective exposure time ($t_{\rm gal}$) and multiplying with $E_{\rm eff}$, giving

$$F_{\text{2-10 keV}} = \frac{C_{\rm bkgsub}}{t_{\rm gal}} \times E_{\rm eff} \quad (2)$$

To finally calculate rest-frame X-ray luminosities, we use luminosity distances, D_L, determined from the systemic redshift of sources given in S20 and apply the k-correction, $k_{\rm corr} = (1+z)^{\Gamma-2.0}$. Therefore, the rest-frame X-ray luminosities in the 2 – 10 keV band ($L_{\text{2-10 keV}}$) are calculated as

$$L_{\text{2-10 keV}} = F_{\text{2-10 keV}} \times 4\pi D_L^2 \, k_{\rm corr} \quad (3)$$

In Section 4.1 we present the X-ray properties of the individual sources that were detected with relatively high S/N.

3.3 Stacking

To boost the S/N of X-ray emission, we perform stacking analysis, where the stacked X-ray luminosity of N sources is calculated as

$$L_X^{\rm stack} = \frac{1}{N} \sum_i^N F_{X,i} \times 4\pi D_{L,i}^2 \, k_{\rm corr} \quad (4)$$

As shown by Fornasini et al. (2019), the above mentioned approximation to stacking works for galaxies that have similar L_X. Since in this study we are probing galaxies with similar physical properties such as redshifts, SFRs and masses, and the luminosities that go into the stack are weighted by the effective exposure time, we do not expect large inaccuracies in the stacked luminosity measured in this way. The errors on luminosity of each source are determined from the errors on the counts, which are then added in quadrature during stacking to obtain errors on the final stacked luminosities measured.

The stacking is performed on two samples of He II emitters. The first sample includes all 18 He II emitters, and the second sample only includes the 13 sources classified as *Narrow* He II emitters (FWHM < 1000 km s^{-1}. The additional sub-sample of only narrow He II emitters is created because as mentioned earlier, explaining the origin of the narrow He II emission line is of particular interest in the context of contribution from X-ray sources. In Section 4.1 we also present the X-ray properties of the stacked He II samples.

3.4 Comparison samples of non-He II emitters

To understand the impact of X-ray sources in He II emitting galaxies, we must compare the X-ray properties of He II emitters with those of non-He II emitters in VANDELS with similar properties such as redshifts, SFRs and stellar masses. For the two samples of He II emitters considered in this study, we create two sub-samples of non-He II emitters that have comparable physical properties to each He II sample.

To build a comparison sample for all He II emitters, we select only those galaxies from VANDELS that lie in the redshift range $2.48 < z < 3.60$, have SFRs in the range $1.03 < \log(\text{SFR}/\text{M}_\odot\text{yr}^{-1}) < 2.19$ and stellar masses in the range $8.78 < \log(\text{M}_\star/\text{M}_\odot) < 9.94$. To create the comparison sample for narrow He II emitters, the physical properties restrictions are $2.48 < z < 3.60$, $1.03 < \log(\text{SFR}/\text{M}_\odot\text{yr}^{-1}) < 2.04$ and $8.78 < \log(\text{M}_\star/\text{M}_\odot) < 9.94$. In Figure 1 we show the normalised histograms of redshifts, SFRs and stellar masses for both classes of He II emitters considered in this study, along with their respective comparison samples.

[3] https://heasarc.gsfc.nasa.gov/docs/software/tools/pimms.html

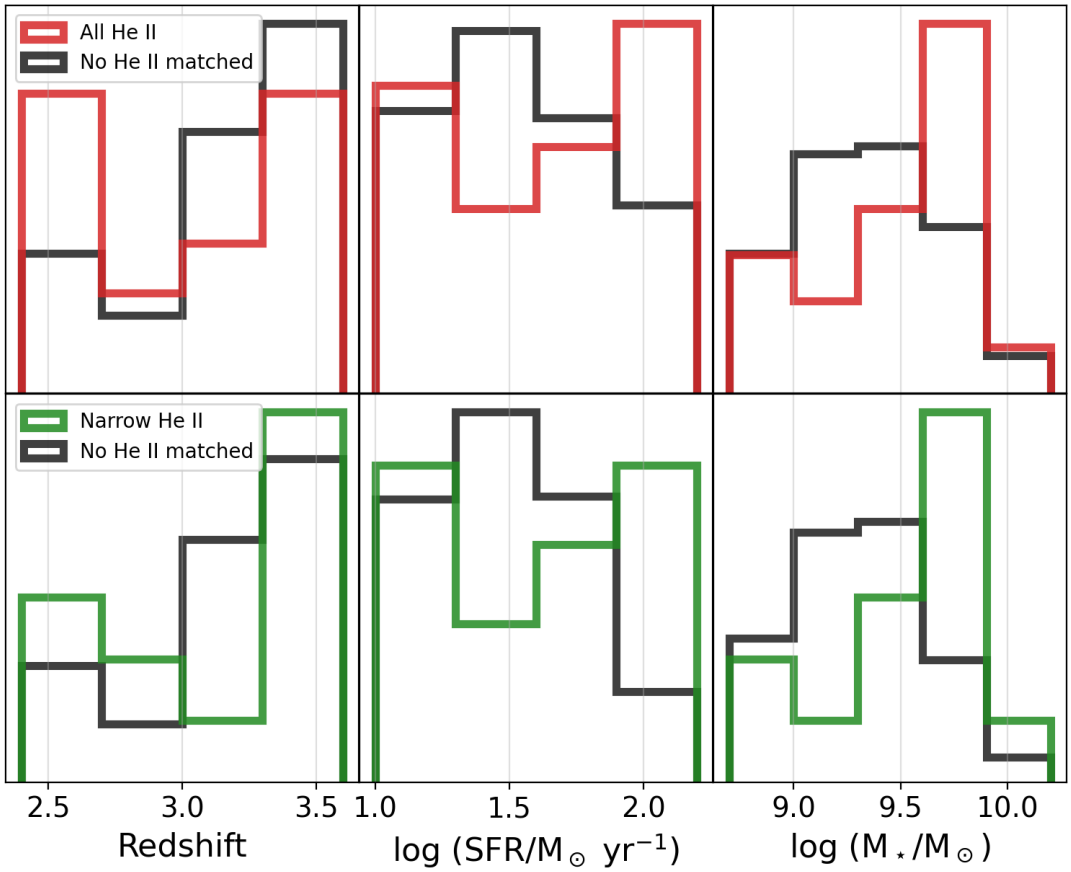

Figure 1. Normalised histograms of redshifts (left), star-formation rates (middle) and stellar masses (right) of the subsets of all He II emitters (top panels) and narrow He II emitters (bottom panels) compared with their respective matched parent samples. The matched samples of galaxies with no He II have been created separately for the two sub-samples of He II emitters to enable a more accurate comparison.

We then identify any strong X-ray sources, most likely X-ray AGN, in the sample of non-He II emitters by matching their coordinates with the CDFS 7 Ms source catalogue from Luo et al. (2017), using a radius of 2 arcseconds. All sources that have a counterpart in the CDFS source catalogue are likely to be AGN and are removed from the comparison sample. Finally, we only consider those sources that lie in a high effective exposure time region in the CDFS 7 Ms image. This results in a total of 318 galaxies with similar physical properties compared to all He II emitters, and 295 galaxies with similar properties compared to narrow He II emitters, that lie within the footprint of the CDFS 7 Ms image.

We ensure comparable effective exposure times in the comparison samples by matching the number of galaxies that are randomly drawn for X-ray photometry from the non-He II emitting galaxy sample. Therefore, to compare with all He II emitters, we randomly draw 18 galaxies from the corresponding comparison sample, and to compare with narrow He II emitters, we draw 13 galaxies from its comparison sample. For the randomly drawn galaxies, X-ray photometry and stacking is performed in a similar fashion to that of He II emitters (described in Section 3.2). This process is bootstrapped, resulting in 500 independent samples for which stacked X-ray luminosities are calculated for the comparison samples of both all and narrow He II emitters. The final stacked X-ray luminosities and the associated errors from the comparison samples are measured from the median and standard deviation of the 500 independent bootstrap iterations.

3.5 X-ray luminosity per SFR (L_X/SFR)

An important quantity that is often used to parametrise the effect of XRBs, primarily the high-mass XRBs, in star-forming galaxies is the X-ray luminosity per unit star-formation rate (L_X/SFR). Lehmer et al. (2016) showed that for star-forming galaxies at $z > 2$ with specific SFRs $> 10^{-8}$ (SFR/M$_\star$), high-mass XRBs are the dominant contributors to the X-ray emissivity. These high-mass XRBs drive the scaling relation between L_X and SFR, as they begin to form only few tens of Myr after a starburst event and therefore, closely trace the star-formation rates (see Antoniou & Zezas 2016, for example).

Since the galaxies in question in this study are all star-forming galaxies at $z > 2$, we also calculate and compare this quantity for both He II emitters and non emitters to capture the contribution of these high-mass XRBs. The dust-corrected SFRs for VANDELS sources are derived from multi-band spectral energy distribution (SED) fitting, as described in McLure et al. (2018). The SFRs for He II emitters along with more details are given in S20.

The stacked L_X/SFR is calculated by dividing the L_X by the SFR for each galaxy that goes into the stack, and the errors are propagated from the X-ray luminosities and added in quadrature. For the purposes of this study we ignore the errors on SFRs, as due to the relatively low X-ray counts expected from the sources, the bulk of the error on L_X/SFR should come from the error on L_X.

4 RESULTS

In this section we present results from X-ray photometry of He II emitters and compare these with results for the bootstrap analysis carried out on the sample of non emitters from VANDELS.

4.1 X-ray counts and luminosities

4.1.1 Individual detections

We find that 4 out of 18 He II emitters have counts with S/N $\geq$ 2 to enable relatively reliable measurements of X-ray fluxes and luminosities. These sources were visually inspected to ensure that the emission is real, and not simply a distribution of noise peaks within the aperture. The background subtracted counts for these sources in the observed energy band 0.8 – 3 keV band range from 7.9 – 14.4, translating into luminosities in the rest-frame 2 – 10 keV band of $L_X = 3.1 - 5.6 \times 10^{41}$ erg s^{-1} (where $X = 2 - 10$ keV). We note that of these 4 sources, 3 were classified as *Bright* He II emitters and one as *Faint* He II emitter by S20 and interestingly, all four sources show narrow He II emission lines (FWHM < 1000 km s^{-1}). The X-ray properties of these individually detected sources along with the measured He II luminosities from S20 are given in Table 2.

Based on the X-ray luminosities of these individually detected sources, we can calculate the He II ionising photon production rate per X-ray luminosity (see Kehrig et al. 2018; Schaerer et al. 2019, for example). To do that, we calculate the He II ionising photon flux, Q(He II), from the total He II luminosity, L(He II), by assuming Case B recombination and electron temperature $T_e = 30000$ K (e.g. Schaerer et al. 2019). We find Q(He II) values in the range $3.0 - 8.7 \times 10^{52}$ photons s^{-1}. Dividing by the X-ray luminosities, we find $q = Q(\text{He II})/L_X$ in the range $5.6 - 15.5 \times 10^{10}$ photons erg^{-1}. These values are higher than what was found for the local dwarf galaxy I Zw 18 by Schaerer et al. (2019), where $q \approx 1.0 - 3.4 \times 10^{10}$ photons erg^{-1}. This suggests that the most X-ray bright sources in our sample of He II emitters may have softer X-ray spectra than what has been observed for I Zw 18, assuming that all of the He II emission is powered by the X-ray sources. The q values measured for the individual sources are also given in Table 2.

4.1.2 Stacks

For the stack of all 18 He II emitters (which include the 4 individually detected He II emitters discussed above), the average background subtracted counts measured are 6.3 ± 2.4, and for the 13 narrow He II emitters, the measured counts are 7.2 ± 2.6. The average background subtracted counts measured for non-He II emitters using bootstrapping are 4.7 ± 0.9 per source, which are lower, but not significantly different than those measured for He II emitters.

We then compare the measured X-ray luminosities in the 2 – 10 keV band from the stacks. We point out that the average redshifts of the two stacks are slightly different, which affects the calculation of the luminosity from the counts. We find that the stack of all He II emitters with an average redshift of $\langle z \rangle = 3.04$ has an X-ray luminosity $\langle L_X \rangle = 2.6 \pm 1.7 \times 10^{41}$ erg s^{-1}. For the matched comparison sample of non-He II emitters, the average redshift across 500 bootstrapped stacks is $\langle z \rangle = 3.15$ and the average luminosity is $\langle L_X \rangle = 2.5 \pm 0.7 \times 10^{41}$ erg s^{-1}.

The stack of narrow He II emitters with a higher average redshift of $\langle z \rangle = 3.33$ have a slightly higher X-ray luminosity $\langle L_X \rangle = 3.1 \pm 1.8 \times 10^{41}$ erg s^{-1}. The matched comparison sample of non-He II emitters, with an average redshift of $\langle z \rangle = 3.19$ has an X-ray luminosity $\langle L_X \rangle = 2.5 \pm 0.9 \times 10^{41}$ erg s^{-1}. The X-ray properties of the stacks are given in Table 3.

In Figure 2 we mark the stacked X-ray luminosity of all He II emitters (left panel) and narrow He II emitters (right panel) against the distribution of X-ray luminosities measured from bootstrapping for their respective comparison samples of non-He II emitters (grey histogram). The black dashed lines indicate the median luminosity inferred from bootstrapping of non-He II emitters, and the dashed coloured lines mark the upper and lower X-ray luminosity confidence intervals for He II emitters.

Our results show that the X-ray luminosities of He II emitting galaxies are marginally higher than that of galaxies with no He II emission. In particular, we find that the stack of narrow He II emitters has the highest X-ray luminosity. However, we note that the X-ray measurements from He II emitters are within 1σ of the distribution of X-ray luminosities from their respective comparison samples of non-He II emitters. To calculate the statistical significance of the X-ray luminosities of He II emitters, we calculate their Z-scores and P-values, which roughly gives the probability of a measurement being a statistical fluctuation from a given distribution. For the stacked luminosity of all He II emitters, we find a Z-score of 0.40, giving a P-value of 0.355, indicating that there is a 35.5% chance of this measurement being a statistical fluctuation and is not significantly different from the distribution of luminosities of non-He II emitters. For the stack of narrow He II emitters, we find a Z-score of 1.45 and a P-value of 0.073, indicating a statistical fluctuation probability of 7.4%. Although the X-ray luminosity of narrow He II emitters lies further away from the median, the inferred P-value still indicates that the difference is not statistically significant ($< 3\sigma$).

From our X-ray measurements, we conclude that although He II emitters, and narrow He II emitters in particular, show marginally higher X-ray luminosities when compared to non-He II emitting galaxies, the difference between the stacked X-ray luminosities of He II emitting and non-emitting galaxy populations is not statistically significant. Therefore, within the statistical uncertainties presented with having small sample sizes, we do not find evidence of enhanced contribution from X-ray sources, presumably X-ray binaries or weak AGN, in galaxies that show the He II emission line at $z \sim 3$. We discuss this implication further in Section 5.

4.2 L_X/SFR

Before calculating L_X/SFR, we note that the median SFRs of the He II emitting galaxies and non-emitting galaxies considered in this study are slightly different. For both stacks of He II emitters, the median SFRs are $\log(\langle \text{SFR} \rangle) \sim 1.7$ M$_\odot$ yr^{-1}, which is higher than the median SFR of galaxies that do not show He II with $\log(\langle \text{SFR} \rangle) \sim 1.5$ M$_\odot$ yr^{-1}. We note once again that the SFRs for all galaxies considered in this study are derived using multi-band SED fitting. For the stack of all He II emitting galaxies, we calculate $\log(\langle L_X \rangle / \langle \text{SFR} \rangle) = 40.03$ erg s^{-1}/($M_\odot$ yr^{-1}), for narrow He II emitters we calculate $\log(\langle L_X \rangle / \langle \text{SFR} \rangle) = 40.11$ erg s^{-1}/($M_\odot$ yr^{-1}), and for galaxies with no He II emission, we calculate $\log(\langle L_X \rangle / \langle \text{SFR} \rangle) = 39.93$ erg s^{-1}/($M_\odot$ yr^{-1}). Similar to X-ray luminosities, we once again find that the L_X/SFR values of He II emitters are marginally higher than non-emitters, but these measurements are not significantly different from each other. Therefore, we conclude that there is no clear excess of L_X/SFR in galaxies that show (narrow) He II emission and those that do not.

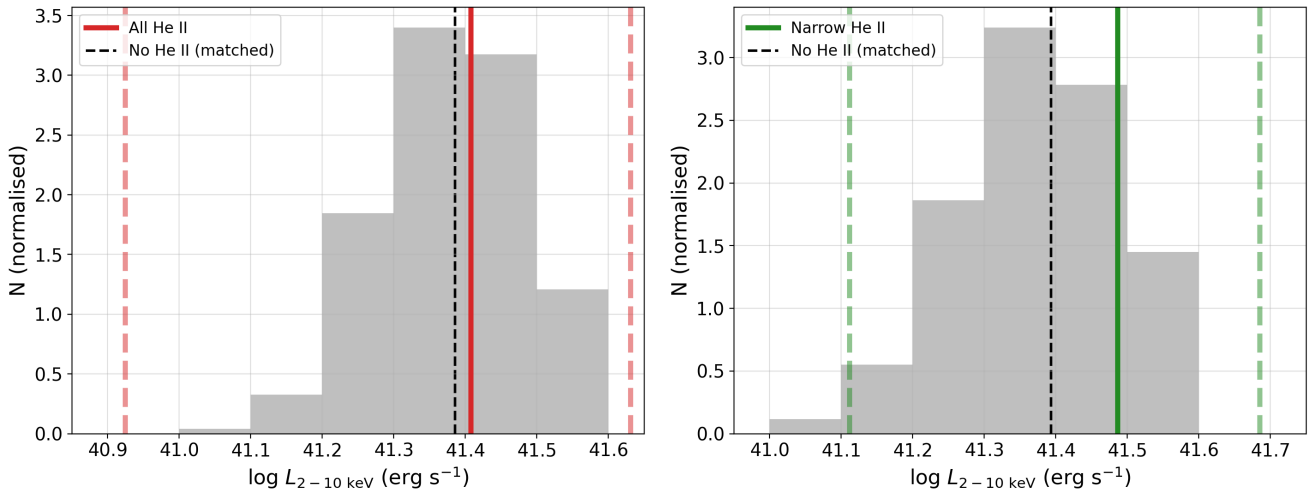

Figure 2. The distribution of stacked X-ray luminosities in the 2 – 10 keV band for the sample of all He II emitters (left) and only narrow (FWHM < 1000 km s^{-1}) He II emitters (right). The distribution in grey shows stacked X-ray luminosity measured from a matched sample of galaxies with no He II emission using bootstrapping in each panel. The dashed lines indicate the upper and lower errors on the measured luminosity of the sample of He II emitters. Although narrow He II emitters show higher X-ray luminosities in comparison, the Z-scores and P-values derived from comparing the stacked luminosities of both classes of He II emitters with the distribution of non-He II emitters shows that the difference between them is not statistically significant at 3σ. This shows that there is no clear X-ray excess in He II emitting galaxies.

Table 2. X-ray properties of individually detected He II emitting sources.

ID	Class	z	C_{bkgsub}	L_X (10^{41} erg s^{-1})	log(SFR) ($M_\odot$ yr^{-1})	log $\frac{L_X}{\mathrm{SFR}}$	$L_{\mathrm{He\,II}}$ (10^{41} erg s^{-1})	$q = \frac{Q(\mathrm{He\,II})}{L_X}$ (10^{10} photons erg^{-1})
CDFS23215	B,N	3.47	9.1 ± 3.0	5.6 ± 1.9	1.3	$40.44^{+0.17}_{-0.27}$	4.9 ± 0.2	15.5 ± 4.5
CDFS113062	B,N	2.69	11.2 ± 3.3	3.1 ± 0.9	1.7	$39.82^{+0.15}_{-0.22}$	2.5 ± 1.2	14.2 ± 3.0
CDFS122687	B,N	2.64	14.4 ± 3.8	3.7 ± 1.0	1.9	$39.60^{+0.13}_{-0.18}$	1.7 ± 0.8	8.2 ± 1.4
CDFS10094	F,N	3.56	7.9 ± 2.9	4.6 ± 1.6	1.7	$39.99^{+0.17}_{-0.29}$	1.5 ± 1.2	5.6 ± 2.7

Class guide: B = *Bright* (S/N(He II) > 2.5), F = *Faint* (S/N(He II) < 2.5), N = *Narrow* (FWHM(He II) < 1000 km s^{-1}), taken from S20.

Table 3. X-ray properties of stacks.

Stack	N	Total exp. (Ms)	$\langle z \rangle$	$\langle C_{\mathrm{bkgsub}} \rangle$	$\langle L_X \rangle$ (10^{41} erg s^{-1})	log$\langle$SFR$\rangle$ ($M_\odot$ yr^{-1})	log $\frac{\langle L_X \rangle}{\langle \mathrm{SFR} \rangle}$
All He II	18	126	3.04	6.2 ± 3.6	2.6 ± 1.7	1.7	$40.01^{+0.26}_{-0.75}$
No He II (matched)*	18	126	3.15	4.3 ± 1.0	2.4 ± 0.7	1.6	$39.95^{+0.12}_{-0.17}$
Narrow He II	13	91	3.33	7.1 ± 3.8	3.1 ± 1.8	1.7	$40.01^{+0.27}_{-0.82}$
No He II (matched)*	13	91	3.19	4.3 ± 1.1	2.5 ± 0.9	1.5	$39.97^{+0.14}_{-0.22}$

*: errors measured on the stack of non-He II emitters are from 500 bootstrap repetitions.

4.2.1 *Redshift evolution*

To place our measurements of L_X/SFR for both He II emitters and non-emitters within the general population of star-forming galaxies at high redshifts, we compare our measurements to those in the literature. We begin by looking at the redshift evolution of L_X/SFR inferred from samples of star-forming galaxies at $z \sim 2$ from Fornasini et al. (2019). In Figure 3 we show models predicting the redshift evolution of L_X/SFR from Lehmer et al. (2016) and Aird et al. (2017), the values measured by Fornasini et al. (2019) at $z \sim 2$, along with our measurements both for individually detected sources and stacks. The shaded region marks the redshift range probed in this study. We note that the redshift evolution models shown essentially capture the 'X-ray main sequence' of star-formation, and have been calibrated using measurements at lower redshifts. The model predictions shown are normalised for star-formation rates of 20 $M_\odot$ yr^{-1} to best match the observations from Fornasini et al. (2019).

We find that our measurement of L_X/SFR for individually detected sources and stacks of both He II emitters and non emitters are consistent with what has been measured for star-forming galaxies at $z \sim 1.5 - 2.5$, and in line with model predictions. Overall, we find little to no evolution in L_X/SFR between redshifts of 2 to 3. However, a proper study that captures the X-ray flux from the entire star-forming population in a systematic fashion is required to more

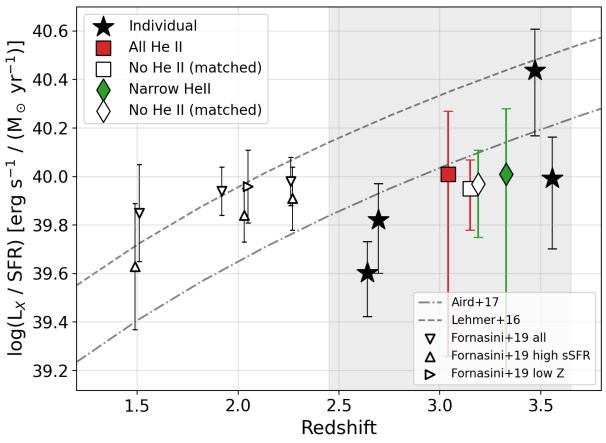

Figure 3. L_X/SFR versus redshift for star-forming galaxies at high redshifts. The coloured symbols show L_X/SFR measured in stacks, and black stars represent individual measurements in He II emitters with the highest S/N in the X-ray image. The open symbols show measurements of lower redshift star-forming galaxies from Fornasini et al. (2019). The shaded region represents the range of redshift of sources that have been stacked in our measurements. We also show redshift evolution predicted by models from Lehmer et al. (2016) and Aird et al. (2017). We do not find a significant difference in L_X/SFR for galaxies with He II and those without. Further, our measurements for both classes of galaxies are consistent with values found at $z \sim 2$.

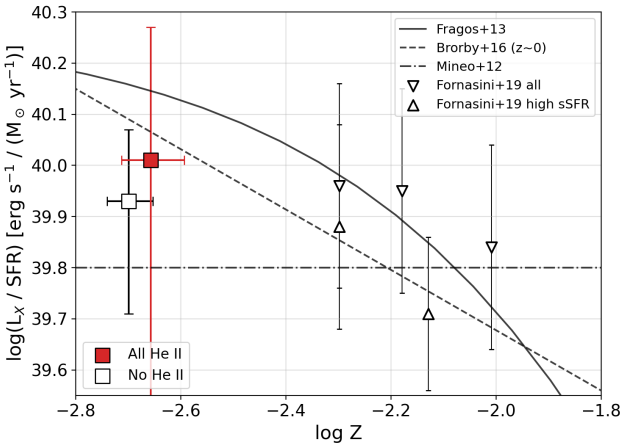

Figure 4. The dependence of L_X/SFR on stellar metallicity. The orange square shows the measurement for all He II emitters, and red circle represents the non-He II emitters. Also shown for comparison are observations from Fornasini et al. (2019) for their samples of star-forming galaxies at $z \sim 2$. Overlaid on top of the observations are predictions of XRB models from Fragos et al. (2013a), in addition to the local relation between L_X/SFR and metallicity observed by Brorby et al. (2016). The metallicities measured for both He II emitters and non-emitters are taken from S20. Our measurements for both classes of galaxies at $z \sim 3$ are comparable with observations at lower redshifts, and also in line with both model predictions and the $z \sim 0$ relation. The assumed solar metallicity here is $\log\ Z = -1.7$.

accurately determine whether or not there is any redshift evolution out to $z \sim 3$.

We note here that a key difference between the L_X/SFR determined for our sample and that of Fornasini et al. (2019) is how the SFRs are measured. For our sources, we rely on SED derived SFRs using photometry at rest-frame UV to optical wavelengths, whereas the SFRs for a majority of sources in the Fornasini et al. (2019) sample are derived using direct measurements of the Hα emission line. Therefore, the timescales of the star-formation rates derived from the SED and the Hα line would be different.

4.2.2 *Dependence on metallicity*

Several studies have explored the dependence of L_X/SFR on stellar metallicity for star-forming galaxies, both from theoretical (Fragos et al. 2013a,b; Madau & Fragos 2017) and observational points of view (Basu-Zych et al. 2013a,b; Brorby et al. 2016; Fornasini et al. 2019). Almost all evidence points towards a negative correlation between L_X/SFR and metallicity, both in the local and high-redshift Universe. This anti-correlation is driven primarily by the presence of higher mass black hole binaries at lower metallicities, that increases the contribution of high-mass XRBs to the overall L_X/SFR measured.

For our He II and non-He II emitting galaxies, we presented stellar metallicity measurements in S20, which were performed by fitting spectral features in the UV spectrum following the method of Cullen et al. (2019). To achieve high enough S/N to enable metallicity measurement, we only used stacks of all He II emitters. Although such methods may not be as accurate as direct metallicity measurements from rest-frame optical emission lines, the stellar metallicities inferred can still provide valuable insights. In the context of predictions from models and previous observational evidence, we now compare whether our L_X/SFR measurements are in line with its dependence on metallicity that has been previously seen.

We once again compare our measurements with those of Fornasini et al. (2019). Note here that Fornasini et al. (2019) use the gas-phase (O/H) ratios derived from spectroscopy as a proxy for stellar metallicity for their sample of star-forming galaxies. Since their metallicity measurements were made using rest-frame optical spectroscopy, they benefit from direct measurements of (O/H) ratios. For ease of comparison, we convert these (O/H) ratios to metal mass-fraction Z, using $Z = (\mathrm{O/H}) * (\mathrm{H_{frac}}/\mathrm{O_{frac}})$, where $\mathrm{H_{frac}}$ is the mass fraction of Hydrogen and $\mathrm{O_{frac}}$ is the mass fraction of Oxygen. We find that assuming 40% of O and 75% of H are trapped in metals gives us consistent values when recovering the solar values for both (O/H) and Z. Our measurements along with observations from Fornasini et al. (2019) are shown in Figure 4. Also shown are the predictions from Fragos et al. (2013a), along with the best-fit power-law to data at $z \sim 0$ from Brorby et al. (2016) and the case of no metallicity dependence of L_X/SFR, as was reported by Mineo et al. (2012).

Our measurements are in agreement with the metallicity dependence predicted by models and what has been reported in the literature. The L_X/SFR for He II emitters is in line with the metallicity dependence predicted from models when compared to the Fornasini et al. (2019) measurements made for galaxies with high specific SFRs. We also note that our measurements at $z \sim 3$ are also consistent with the metallicity dependence of L_X/SFR measured in the local Universe by Brorby et al. (2016). Given the relatively large error bars on the stacked luminosities determined for galaxies in this work, our results are also consistent with a scenario where there is little to no evolution in the L_X/SFR with metallicity as reported

by Mineo et al. (2012). In a future study we aim to explore this metallicity dependence in more detail, extending the analysis to the full VANDELS sample of star-forming galaxies.

As Saxena et al. (2020) noted, there is a slight caveat of the stellar metallicity measurement method from Cullen et al. (2019) used in their work. With this method, the template fitting used to determine stellar metallicities from features in the rest-frame UV spectra assumes a constant star-formation history. This assumption is valid for averaging across the general star-forming galaxy population at high redshifts, but if galaxies (for example those with He II) are very young, then their true metallicities may be higher than what is inferred using this method.

5 DISCUSSION

5.1 No evidence of enhanced XRB contribution in He II emitters

We find that the differences between L_X and L_X/SFR of He II emitters and non-emitters are not statistically significant. These results suggest that there is no excess X-ray emission, of whatever origin, in galaxies that show strong He II emission in their spectra. As shown in S20, the metallicities measured for both He II emitters and non-emitters are comparable too, in addition to physical properties such as stellar mass and star-formation rates. Since the L_X/SFR we measure for both classes of galaxies are also consistent with models and predictions for the general star-forming galaxy populations, we find that there is no discernible difference in either the X-ray emission or other physical properties of galaxies that show He II .

We can also test whether there is any correlation between the strength of He II emission line and the X-ray luminosity of individually detected sources by exploring whether L_X/SFR correlates with the observed EW of the He II emission line. Shown in Figure 5 are L_X/SFR measurements and limits for all individual He II emitters. We colour code the sources, with *Bright* (S/N (He II) > 2.5) He II emitters shown in blue and *Faint* (S/N (He II) < 2.5) He II emitters shown in orange. Those sources that have individual X-ray detections presented in Table 2 are marked using stars. Although looking at only the brightest individual X-ray detections may suggest that L_X/SFR weakly correlates with He II EW, the overwhelming majority of X-ray non-detected He II emitters with comparable EWs suggests that there is no clear correlation between the strength of the He II emission line and L_X/SFR measured in the galaxy. This is best highlighted by the highest EW He II emitting galaxy not being detected in the X-ray image.

Our findings are comparable to what was reported by Senchyna et al. (2020), who found no strong correlation between L_X/SFR and He II /Hβ ratios for a small sample of nearby galaxies either, leading them to conclude that high-mass XRBs are not the dominant sources of He II ionising photon production. However, our results appear to be inconsistent with the findings of Lebouteiller et al. (2017), Schaerer et al. (2019) and Heap et al. (2019), who reported that contribution from XRBs in the well-studied metal-poor galaxy in the local Universe, I Zw 18, can account for the nebular He II (λ4686) seen in its spectrum. These studies also showed that the X-ray luminosities observed in this galaxy are in line with the metallicity-dependence of XRBs.

The lack of excess X-ray emission from galaxies that show He II emission in their UV spectra compared to those that do not, suggests that within the scope of this analysis, we do not find evidence of high-mass XRBs being the dominant sources of He II ionising photon production in $z \sim 3$ galaxies. Although the narrow

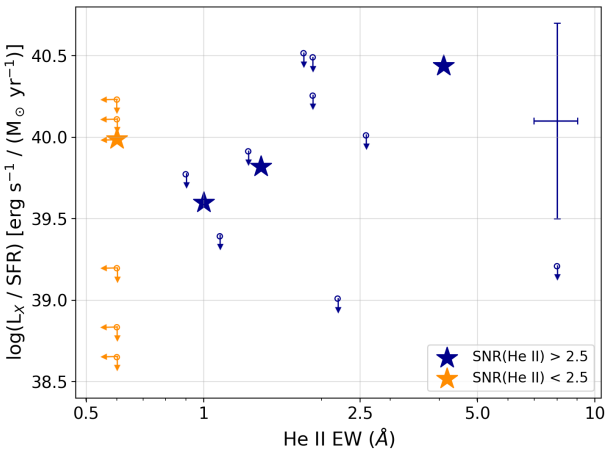

Figure 5. L_X/SFR as a function of He II EW for both *Bright* (blue) and *Faint* (orange) He II emitters from the sample of S20. The individual galaxies with S/N > 2 in the X-ray image are marked with stars and 2σ limits are marked using downward pointing arrows. The average errors on L_X/SFR and He II EWs are shown in the top-right. It is clear that for He II emission with comparable EWs, the measured L_X/SFR spans more than an order of magnitude. This suggests that there is no clear correlation between L_X/SFR and He II EW, leading to the conclusion that XRBs are not universally dominant in He II emitting galaxies.

He II emitting galaxies do show a marginal excess in X-ray emission when compared to the sample of non emitters, with the current data (and limits on errors) available we can not conclude for certain whether this excess is statistically significant. Since the CDFS 7 Ms data is the deepest X-ray data available in any extragalactic field, the step forward might be to reduce error bars on X-ray measurements from He II emitters through the identification of a much larger sample of He II emitting galaxies.

5.2 Presence of obscured AGN?

The photon energies required to ionise He II ($E > 54$ eV) are easily produced in the accretion disks of active galactic nuclei (AGN) across redshifts. However, the presence of AGN in high-redshift galaxies leads to the excitation of other emission lines that also require extremely high energy photons, in addition to brightness at radio and X-ray wavelengths. S20 used radio or X-ray detections, as well as detection of C IV in emission to identify possible AGN from the sample of He II emitters and these AGN were removed from the analysis and the stacks presented in this study (even though the presence of both He II and C IV can be explained using some stellar models without the need for AGN). With the addition of deeper X-ray photometry, we can explore whether weaker or obscured AGN could still be present in the sample of He II emitters.

Thanks to the choice of observing band (0.8 – 3 keV) and the redshift of our sources, the strong Fe Kα emission line at a rest-frame energy of 6.4 keV, often associated with reflection of X-ray emission from the accretion disk of the AGN (e.g. Lightman & White 1988), is in principle observable for our sample. Ricci et al. (2014) showed that the Fe Kα line is observed both in obscured and unobscured AGN. Therefore, if the He II emission seen in the UV spectra of certain sources is indeed originating from the central AGN in galaxies, we can expect to see some contribution of the

generally bright Fe Kα line at X-ray wavelengths probed in this study too. Comparing the X-ray counts and luminosities of samples of He II emitting and non-emitting galaxies, we already showed that there is no statistically significant difference between the two. Therefore, in the context of emission from AGN, this means that there is no clear contribution from the Fe Kα line to the X-ray luminosity of He II emitters. In combination with the lack of other clear AGN signatures in the spectra of He II galaxies presented in S20, we can conclude that the scenario where faint or obscured AGN are powering the He II emission seen is unlikely.

Depending on the stacked X-ray luminosities determined for various classes of He II emitters, we can calculate the likelihood of the presence of obscured AGN based on luminosity functions from the literature (e.g. Aird et al. 2015; Buchner et al. 2015). Vito et al. (2018) extended such studies to fainter X-ray luminosities and calculated the fraction of obscured AGN both as a function of X-ray luminosity as well as redshift using the Chandra 7Ms image. Vito et al. (2018) showed that this fraction drops rapidly at luminosities below $L_{2\text{-}10\,\mathrm{keV}} = 10^{43}$ erg s^{-1} in the redshift range $z = 3 - 6$ (however, their sample is incomplete below this luminosity limit too). The stacked X-ray luminosities measured for our He II emitting sample are in the range $L_{2\text{-}10\,\mathrm{keV}} = 10^{41.4-41.5}$ erg s^{-1}, and based on this tentative drop in the fraction of obscured AGNs at low X-ray luminosities, the likelihood of presence of obscured AGNs in the He II emitting sample is considerably reduced. Further, Circosta et al. (2019) showed that even obscured AGN at $z > 2.5$ can have X-ray luminosities in excess of $L_X > 10^{44}$ erg s^{-1}, which is much larger than the luminosities we find for He II emitting sources in this study.

5.3 Other possible explanations for He II

Apart from XRBs and AGN, there may be localised high-mass star-formation occurring in certain regions of the galaxy that could be powering the He II emission that is observed in the UV spectra. For high-redshift galaxies, the SED inferred physical properties (with limited resolution and sensitivity) tend to get averaged over the entire galaxy. Therefore, the similar metallicities and X-ray luminosities of galaxies that show He II emission and those that do not suggest that the physical properties of both these classes of objects are largely similar. However, some differences in stellar populations are needed to explain the He II emission in some galaxies. Since L_X/SFR of star-forming galaxies is dependent on metallicity (although with some scatter), it may be possible that there are localised regions of high-mass, low-metallicity star formation, possibly also hosting more XRBs, within He II emitting galaxies. S20 showed that the stacked rest-frame UV spectrum of all He II emitting galaxies has stronger nebular emission lines when compared to the stack of non-He II emitters, suggesting recent star-formation activity. However, the metallicities measured for both classes of objects were found to be comparable. A scenario where pockets of low-mass star-formation regions are present in a galaxy with an overall evolved stellar population, which ultimately power the He II (and other nebular) emission cannot be ruled out. Since the X-ray luminosities measured from the CDFS image also encapsulate emission from the entire galaxy, it is impossible to study any spatial effect in the X-rays for the He II emitting galaxies.

Unfortunately the age-metallicity degeneracy cannot be broken using the Cullen et al. (2019) method, as it relies on an assumption of constant star-formation over a timescale of 100 Myr. Future observations of rest-frame optical lines for comparable samples of He II emitters and non-emitters may offer accurate measurements of has phase metallicities and stellar ages, and shed some light on the underlying differences in their star-formation histories.

In the local Universe where galaxies are spatially resolved, it is possible to directly study the spatial overlap between He II emission, regions of intense star-formation and/or X-ray point sources. Kehrig et al. (2018) studied X-ray emission from the metal-poor starburst galaxy SB0335-052E showing He II λ4686 emission in the local Universe, reporting that the low X-ray luminosities of point sources detected within the galaxy effectively rule out significant contribution from XRBs to the He II ionising budget, even though X-ray sources are spatially coincident with the He II emitting regions. Kehrig et al. (2018) concluded that ionisation by single metal-free stars or binary stars with $Z \sim 10^{-5}$ with a top-heavy initial-mass function in current stellar population models is the most likely explanation for the He II emission observed in this particular galaxy. However, Schaerer et al. (2019) suggested that beaming effects on X-ray emission, which result in relatively low observed X-ray fluxes but do not rule out contribution from XRBs towards the He II ionising budget, may offer an explanation.

As argued by S20, even though it remains unclear whether XRBs are the dominant producers of He II ionising photons or not, binary-star models (Eldridge et al. 2017) overall do a better job at producing more He II ionising photons compared to single star models (see also Steidel et al. 2016). Recent modelling of production of ionising radiation in star-forming galaxies by Plat et al. (2019) showed that the highest He II EWs are produced in low-metallicity stellar populations (both single and binary-star models) with high ionisation parameter values, log $U \geq -2$. However, to explain the highest He II EWs observed in the literature, the stellar populations must have very young ages (log age/yr < 7). Plat et al. (2019) also showed that although contribution from XRBs could play a role, they may not be the dominant sources of He II ionisation. Improvements in the predicted number of photons and inclusion of other physical phenomena associated with the evolution of massive (binary) stars, such as inclusion of massive stars whose outer envelope has been stripped due to binary interactions exposing a helium core (Götberg et al. 2018, 2019) may be needed to match the observed He II EWs at high redshifts.

It may also be possible that small pockets of metal-free, Pop III-like stars exist within galaxies that show that strong He II emission (Tumlinson et al. 2001; Schaerer 2003; Scannapieco et al. 2003). Pop III stars, in combination with a more widespread population of Pop II (metal-enriched) stars, may be able to explain the bright He II emission seen in high redshift galaxies (e.g. Visbal et al. 2017). We note, however, that not all strong He II emitters in the S20 sample show a strong Lyα emission line, which is an important requirement for ionisation by Pop III-like stars. Additionally, a population of very massive stars (VMS) at low metallicities could be capable of producing the narrow He II emission line, primarily due to strong but slower Wolf-Rayet type stellar winds (Gräfener & Vink 2015).

Finally, fast radiative shocks are known to be capable of powering high-ionisation emission lines in local, metal-poor galaxies (e.g. Thuan & Izotov 2005; Izotov et al. 2012) and such shocks may also play an important role in powering the narrow He II emission seen in star-forming galaxies at high redshifts. However, isolating the impact of radiative shocks requires using the classical BPT diagnostics (Baldwin et al. 1981), and observations of rest-frame optical emission lines of He II emitting galaxies at high redshifts using the *James Webb Space Telescope* may shed some light on the effects of shocks in these galaxies.

6 SUMMARY AND CONCLUSIONS

Building upon the sample of He II λ1640 emitting galaxies at $z \sim 2.2-5$ presented in S20, in this study we have presented their X-ray properties. We have used the *Chandra* 7 Ms X-ray data in the CDFS field, which is the deepest X-ray data set available in a well studied extragalactic field.

We have performed aperture photometry at the locations of He II emitting galaxies to determine their X-ray fluxes. To boost the effective exposure times and infer the average X-ray properties of the population of He II emitting galaxies, we have also employed stacking analysis to calculate stacked X-ray luminosities of the He II emitting sample. To put the X-ray properties of He II emitting galaxies in context, we have performed a bootstrap analysis to determine the X-ray properties of galaxies with no He II emission in their UV spectra, but with comparable physical properties and redshifts to those that show He II . The main conclusions of this study are as follows:

- For individual galaxies with S/N > 2 in X-rays, we find luminosities in the range $L_{2\text{-}10\,\mathrm{keV}} = 3.1 - 5.6 \times 10^{41}$ erg s^{-1}. By calculating the He II ionising photons produced per X-ray luminosity, we find that X-ray binaries (XRBs) are not capable of fully powering the He II emission line.
- Using stacking analysis, we find the stacked X-ray luminosity of all 18 He II emitters in the sample to be $L_{2\text{-}10\,\mathrm{keV}} = 2.6 \times 10^{41}$ erg s^{-1}, and for the 13 narrow (FWHM(He II)< 1000 km s^{-1}) He II emitters to be $L_{2\text{-}10\,\mathrm{keV}} = 3.1 \times 10^{41}$ erg s^{-1}. We then calculate the distribution of X-ray luminosities from randomly drawn samples of non-He II emitting galaxies using bootstrapping, that are matched in numbers to the stacks of all and narrow He II emitters. We find that although the stacked X-ray luminosity of He II emitting galaxies is marginally higher than that of galaxies with no He II , the difference is not statistically significant. Therefore, we find no evidence of enhanced X-ray emission in star-forming galaxies that show He II emission in their spectra at $z \sim 3$.
- To study what this result means for the impact of XRBs in He II emitting galaxies, we compare the X-ray luminosity per star-formation rate (L_X/SFR) for galaxies with and without He II . We find that L_X/SFR measured for stacks of He II emitters are marginally higher than that measured for galaxies with no He II emission, but these values are not significantly different and consistent within the error bars.
- The redshift evolution and metallicity dependence of L_X/SFR measured in our stacks is consistent with what has been reported in the literature at lower redshifts. Our measurements at $z \sim 3$ are compatible with models predicting the redshift evolution of L_X/SFR based on the 'X-ray main sequence' of star-forming galaxies, and we find little to no redshift evolution observed between $z \sim 2-3$. The metallicity dependence of L_X/SFR we find for He II emitters is consistent also consistent with little to no evolution at the lowest metallicity values.
- We find no clear correlation between L_X/SFR measured for individually X-ray detected He II emitters, and the equivalent width of He II emission seen in these galaxies. We show that most of the bright He II emitters do not show any X-ray detection. Therefore, we conclude that there is no increased contribution from XRBs in galaxies that show He II at $z \sim 3$.
- In the light of these X-ray measurements, we discuss some additional mechanisms that could be powering He II in some galaxies. Given the low values of L_X inferred from stacks of both He II emitters and non-emitters, we argue that even weak or obscured AGNs can be ruled out. Therefore, the He II emission could either be powered by localised high-mass star-formation, very high mass single or binary stars with low metallicities, viewing angle effects from XRBs or radiative shocks.

To differentiate between the various underlying mechanisms that are possibly powering galaxies showing He II emission at high redshifts, a multi-wavelength approach is essential. For example, access to rest-frame optical spectra with high S/N can help determine the physical properties of the stellar populations and enable more accurate metallicity measurements for He II emitting galaxies. Follow-up observations with high-spatial resolution, both through imaging and spectroscopy, may help isolate regions of enhanced star-formation in these galaxies that could be powering the strong He II emission lines observed. Improvements to modelling the origin of radiation from massive (binary) stars and including them in stellar population synthesis codes may also bring us closer to addressing the missing He II ionising photons problem. Observations with upcoming facilities such as the *James Webb Space Telescope* and the *Extremely Large Telescope* may reveal answers to pressing questions surrounding the production of high energy photons from stars that ultimately escape from galaxies in the very early Universe and drive the process of reionisation.

ACKNOWLEDGEMENTS

The authors thank the referee for useful comments and suggestions that improved the quality of this work. AS and LP would like to thank Fabrizio Fiore, Simonetta Puccetti, Andrea Ferrara and Roberto Maiolino for their valuable input. AS would like to thank Richard Ellis for useful discussions and suggestions. AC acknowledges the support from grant PRIN MIUR 2017-20173ML3WW_001 and ASI n.2018-23-HH.0. This work has made extensive use of JUPYTER and IPYTHON (Pérez & Granger 2007), ASTROPY (Astropy Collaboration et al. 2013), MATPLOTLIB (Hunter 2007) and TOPCAT (Taylor 2005). This work would not have been possible without the countless hours put in by members of the open-source developing community all around the world.

DATA AVAILABILITY

The data underlying this article are part of VANDELS, which is a European Southern Observatory (ESO) Public Spectroscopic Survey. The data can be accessed using the VANDELS database at `http://vandels.inaf.it/dr3.html`, or through the ESO archives. The code used to perform the analysis in this paper will be shared on reasonable request to the corresponding author.

REFERENCES

Aird J., Coil A. L., Georgakakis A., Nandra K., Barro G., Pérez-González P. G., 2015, MNRAS, 451, 1892
Aird J., Coil A. L., Georgakakis A., 2017, MNRAS, 465, 3390
Amorín R., et al., 2017, Nature Astronomy, 1, 0052
Antoniou V., Zezas A., 2016, MNRAS, 459, 528
Astropy Collaboration et al., 2013, A&A, 558, A33
Baldwin J. A., Phillips M. M., Terlevich R., 1981, PASP, 93, 5
Basu-Zych A. R., et al., 2013a, ApJ, 762, 45
Basu-Zych A. R., et al., 2013b, ApJ, 774, 152
Berg D. A., Skillman E. D., Henry R. B. C., Erb D. K., Carigi L., 2016, ApJ, 827, 126

Berg D. A., Erb D. K., Auger M. W., Pettini M., Brammer G. B., 2018, ApJ, 859, 164
Berg D. A., Chisholm J., Erb D. K., Pogge R., Henry A., Olivier G. M., 2019, ApJ, 878, L3
Bouwens R. J., Illingworth G. D., Oesch P. A., Caruana J., Holwerda B., Smit R., Wilkins S., 2015, ApJ, 811, 140
Bradley L., et al., 2019, astropy/photutils: v0.6, doi:10.5281/zenodo.2533376, https://doi.org/10.5281/zenodo.2533376
Brinchmann J., Kunth D., Durret F., 2008, A&A, 485, 657
Bromm V., Larson R. B., 2004, ARA&A, 42, 79
Bromm V., Yoshida N., 2011, ARA&A, 49, 373
Brorby M., Kaaret P., Prestwich A., Mirabel I. F., 2016, MNRAS, 457, 4081
Bruzual G., Charlot S., 2003, MNRAS, 344, 1000
Buchner J., et al., 2015, ApJ, 802, 89
Calzetti D., Armus L., Bohlin R. C., Kinney A. L., Koornneef J., Storchi-Bergmann T., 2000, ApJ, 533, 682
Cassata P., et al., 2013, A&A, 556, A68
Circosta C., et al., 2019, A&A, 623, A172
Cullen F., et al., 2019, MNRAS, 487, 2038
Dopita M. A., Sutherland R. S., 1996, ApJS, 102, 161
Douna V. M., Pellizza L. J., Mirabel I. F., Pedrosa S. E., 2015, A&A, 579, A44
Eldridge J. J., Stanway E. R., Xiao L., McClelland L. A. S., Taylor G., Ng M., Greis S. M. L., Bray J. C., 2017, Publ. Astron. Soc. Australia, 34, e058
Fornasini F. M., et al., 2019, ApJ, 885, 65
Fragos T., et al., 2013a, ApJ, 764, 41
Fragos T., Lehmer B. D., Naoz S., Zezas A., Basu-Zych A., 2013b, ApJ, 776, L31
Garnett D. R., Kennicutt Robert C. J., Chu Y.-H., Skillman E. D., 1991, ApJ, 373, 458
Gehrels N., 1986, ApJ, 303, 336
Giallongo E., et al., 2019, ApJ, 884, 19
Götberg Y., de Mink S. E., Groh J. H., Kupfer T., Crowther P. A., Zapartas E., Renzo M., 2018, A&A, 615, A78
Götberg Y., de Mink S. E., Groh J. H., Leitherer C., Norman C., 2019, A&A, 629, A134
Gräfener G., Vink J. S., 2015, A&A, 578, L2
Grogin N. A., et al., 2011, ApJS, 197, 35
Guseva N. G., Izotov Y. I., Thuan T. X., 2000, ApJ, 531, 776
Gutkin J., Charlot S., Bruzual G., 2016, MNRAS, 462, 1757
Heap S. R., Hubeny I., Lanz T. M., 2019, Stars and Stellar Black Holes in the Low-metallicity Galaxy I Zw 18. p. 267
Henry A., et al., 2013, ApJ, 776, L27
Hunter J. D., 2007, Computing In Science & Engineering, 9, 90
Izotov Y. I., Thuan T. X., 2004, ApJ, 602, 200
Izotov Y. I., Thuan T. X., Privon G., 2012, MNRAS, 427, 1229
Kehrig C., et al., 2011, A&A, 526, A128
Kehrig C., Vílchez J. M., Pérez-Montero E., Iglesias-Páramo J., Brinchmann J., Kunth D., Durret F., Bayo F. M., 2015, ApJ, 801, L28
Kehrig C., Vílchez J. M., Guerrero M. A., Iglesias-Páramo J., Hunt L. K., Duarte-Puertas S., Ramos-Larios G., 2018, MNRAS, 480, 1081
Koekemoer A. M., et al., 2011, ApJS, 197, 36
Lebouteiller V., et al., 2017, A&A, 602, A45
Lehmer B. D., et al., 2016, ApJ, 825, 7
Lightman A. P., White T. R., 1988, ApJ, 335, 57
Linden T., Kalogera V., Sepinsky J. F., Prestwich A., Zezas A., Gallagher J. S., 2010, ApJ, 725, 1984
Luo B., et al., 2017, ApJS, 228, 2
Madau P., Fragos T., 2017, ApJ, 840, 39
Magliocchetti M., et al., 2020, MNRAS, 493, 3838
McLure R. J., et al., 2018, MNRAS, 479, 25
Mignoli M., et al., 2019, A&A, 626, A9
Mineo S., Gilfanov M., Sunyaev R., 2012, MNRAS, 419, 2095
Nanayakkara T., et al., 2019, A&A, 624, A89
Oke J. B., Gunn J. E., 1983, ApJ, 266, 713
Patrício V., et al., 2016, MNRAS, 456, 4191
Pentericci L., et al., 2018, A&A, 616, A174
Pérez F., Granger B. E., 2007, Computing in Science and Engineering, 9, 21
Planck Collaboration et al., 2016, A&A, 594, A13
Plat A., Charlot S., Bruzual G., Feltre A., Vidal-García A., Morisset C., Chevallard J., Todt H., 2019, MNRAS, 490, 978
Ricci C., Ueda Y., Paltani S., Ichikawa K., Gand hi P., Awaki H., 2014, MNRAS, 441, 3622
Robertson B. E., Ellis R. S., Dunlop J. S., McLure R. J., Stark D. P., 2010, Nature, 468, 49
Robertson B. E., Ellis R. S., Furlanetto S. R., Dunlop J. S., 2015, ApJ, 802, L19
Sanders R. L., et al., 2018, ApJ, 858, 99
Saxena A., et al., 2020, A&A, 636, A47
Scannapieco E., Schneider R., Ferrara A., 2003, ApJ, 589, 35
Schaerer D., 1996, ApJ, 467, L17
Schaerer D., 2003, A&A, 397, 527
Schaerer D., Fragos T., Izotov Y. I., 2019, A&A, 622, L10
Senchyna P., et al., 2017, MNRAS, 472, 2608
Senchyna P., Stark D. P., Mirocha J., Reines A. E., Charlot S., Jones T., Mulchaey J. S., 2020, MNRAS, 494, 941
Shirazi M., Brinchmann J., 2012, MNRAS, 421, 1043
Stanway E. R., Eldridge J. J., 2018, MNRAS, 479, 75
Stanway E. R., Eldridge J. J., 2019, A&A, 621, A105
Stanway E. R., Eldridge J. J., Becker G. D., 2016, MNRAS, 456, 485
Stasińska G., Izotov Y., Morisset C., Guseva N., 2015, A&A, 576, A83
Steidel C. C., et al., 2014, ApJ, 795, 165
Steidel C. C., Strom A. L., Pettini M., Rudie G. C., Reddy N. A., Trainor R. F., 2016, ApJ, 826, 159
Szécsi D., Langer N., Yoon S.-C., Sanyal D., de Mink S., Evans C. J., Dermine T., 2015, A&A, 581, A15
Taylor M. B., 2005, in Shopbell P., Britton M., Ebert R., eds, Astronomical Society of the Pacific Conference Series Vol. 347, Astronomical Data Analysis Software and Systems XIV. p. 29
Thuan T. X., Izotov Y. I., 2005, ApJS, 161, 240
Tumlinson J., Giroux M. L., Shull J. M., 2001, ApJ, 550, L1
Visbal E., Bryan G. L., Haiman Z., 2017, MNRAS, 469, 1456
Vito F., et al., 2018, MNRAS, 473, 2378
Wise J. H., Demchenko V. G., Halicek M. T., Norman M. L., Turk M. J., Abel T., Smith B. D., 2014, MNRAS, 442, 2560
Xiao L., Stanway E. R., Eldridge J. J., 2018, MNRAS, 477, 904
van de Voort F., Schaye J., Altay G., Theuns T., 2012, MNRAS, 421, 2809

This paper has been typeset from a TEX/LATEX file prepared by the author.